Large-Eddy Simulation of a Wankel Rotary Engine for Range Extender Applications

X Shen[1], AW Costall[1]*, M Turner[1], R Islam[1], A Ribnishki[1], JWG Turner[2], G Vorraro[2], N Bailey[3], S Addy[3]

1: Institute for Advanced Automotive Propulsion Systems (IAAPS), University of Bath, Claverton Down, BA2 7AY, United Kingdom
2: Clean Combustion Research Center (CCRC), King Abdullah University of Science and Technology (KAUST), Thuwal, Saudi Arabia
3: Advanced Innovative Engineering (UK) Limited, Lichfield, United Kingdom

*Corresponding author
Email: awc34@bath.ac.uk

ABSTRACT

The Wankel rotary engine offers unrivalled power density as a consequence of having a combustion event every revolution, as well as lightness, compactness and vibrationless operation due to its perfect balance. These attributes have led to its success as a powerplant for unmanned aerial vehicles, and which should also make it an attractive proposition for range-extended electric vehicles. However, it is not currently in production for automotive applications having historically struggled with poor combustion efficiency, and high fuel consumption and hydrocarbon emissions. The purpose of this work is to study the in-chamber flow motion in order to better understand how such limitations may be overcome in future. A 225cc 30 kW Wankel rotary engine is modelled using Large-Eddy Simulation (LES) to ensure turbulent flow features are faithfully recreated, since Reynolds-averaged Navier-Stokes-based approaches are insufficient in this regard. The LES-predicted peak chamber pressure lies within 3.7% of the engine test data, demonstrating good model validation. Combustion simulation parameters are calibrated to match the measured heat release profile, for high-load engine operation at 4000 rpm. Simulation results provide insight into the generation of turbulent structures as the incoming flow interacts with the throttle, intake port, rotor and housing surfaces; how the turbulence breaks down as the combustion chamber is compressed; and how the flame propagates following ignition, leaving a pocket of reactants unburned. Indeed, the computational approach described here allows detailed understanding of the impact of design parameters on the detailed in-chamber flow phenomena, and consequently engine performance and emissions. This will enable the optimization of Wankel rotary engine geometry, port and ignition timing for maximum combustion efficiency and low emissions, reasserting its potential as an effective and efficient prime mover for hybrid and range extended electric vehicles.

NOMENCLATURE

N	Engine speed
p	Pressure
Q	Q-criterion, Q-criterion, $\frac{1}{2}(\|\boldsymbol{\Omega}\|^2 - \|\boldsymbol{S}\|^2)$
V	Volume

Abbreviations

AIE	Advanced Innovative Engineering
APC	Advanced Propulsion Centre
ATDC	After Top Dead Centre
BEV	Battery Electric Vehicle
BSFC	Brake Specific Fuel Consumption
BTDC	Before Top Dead Centre
CFD	Computational Fluid Dynamics
DES	Detached-Eddy Simulation
FCEV	Fuel Cell Electric Vehicle
HC	Hydrocarbon
HEV	Hybrid Electric Vehicle
HPC	High Performance Computing
ICE	Internal Combustion Engine
LES	Large-Eddy Simulation
NVH	Noise, Vibration, Harshness
RANS	Reynolds-Averaged Navier-Stokes
REEV	Range-Extended Electric Vehicle
TDC	Top Dead Centre
UAV	Unmanned Aerial Vehicle
UDF	User Defined Function

1 INTRODUCTION

The electrification of transport is continuing apace. The consensus, laid down in the form of propulsion technology roadmaps (e.g., 1), is that decarbonization of urban mobility requires an entirely electric fleet, comprising battery electric vehicles (BEVs) and, later on, fuel cell electric vehicles (FCEVs). Yet the same roadmaps recognize that internal combustion engines (ICEs), in the guise of conventional and especially hybrid electric vehicles (HEVs), have an important supporting role in the transition to an electrified future. This is because the transition can only take place over decades, due to the low baseline level of electric vehicle ownership and the slow rate of vehicle renewal. These factors may be illustrated by considering, for example, that of the 15.5M new passenger cars registered in the EU in 2019, 90% still employed a conventional gasoline or diesel ICE (98.1% if hybrids and alternative fuels are included) (2), while the average lifespan of a gasoline passenger car in Germany is around 18 years (3). Indeed, the Advanced Propulsion Centre Light Duty Vehicle Roadmap (1) uses a 30-year-plus timescale, out to beyond 2050.

So, although the electrified transition has begun, the automotive industry is still quite near the start. In the marketplace, consumer concerns over electric vehicle range and the high initial vehicle cost (largely due to the need to accommodate a sufficiently large battery for acceptable range) continues to inhibit uptake of BEVs. This is where HEVs, or range-extended electric vehicles (REEVs), can encourage fleet renewal by offering some of the advantages of electric propulsion (and while using a smaller, lighter, less expensive battery) without the issue of range anxiety. It is therefore essential that the automotive industry continues to advance engine technology in the interest of greater thermal efficiency, and thus lower CO_2 and pollutant emissions, because it is also the consensus that ICEs will persist, in one form or another, for at

least the next three decades. Moreover, they are expected to be present beyond 2050 in long range, high power and performance vehicles, powered by dedicated hybrids running on net zero carbon fuels (1).

1.1 The Wankel rotary engine as a range extender

Although the Wankel rotary engine found mixed success as a prime mover for ground vehicles[1], it is currently in series production as the powerplant for unmanned aerial vehicles (UAVs), which take advantage of characteristics that differentiate it from reciprocating engines, e.g.,

- Perfect balance and hence vibrationless operation
- No noise, vibration, and harshness (NVH) caused by a conventional valve train
- Compactness and lightness, and hence high volumetric and mass power density
- Low friction
- Low rotational inertia

These same attributes make it a strong contender for the prime mover in a dedicated hybrid powertrain for REEVs, if its traditional weaknesses can be improved:

1. High fuel consumption at part- and especially low-load
2. High hydrocarbon (HC) emissions
3. High oil consumption
4. High combustion chamber surface area-to-volume ratio
5. High coolant and exhaust heat rejection
6. Poor combustion chamber shape

Item 1 in the above list can be avoided in a REEV application since the engine is not connected to the drivetrain and may, in the main, be operated at its best fuel efficiency point when running.

In response to item 2, though Wankel rotary engines have a reputation for high HC emissions, the authors' previous work (4) showed that the *side-ported* 13B-MSP RENESIS Wankel rotary engine (5) used in the Mazda RX-8 (homologated at Euro 4) was able to meet more modern (Euro 5 & 6) HC emissions limits, highlighting the value of zero port overlap in inhibiting the escape of unburnt reactants into the exhaust. Follow-on work (6) extended the experimental investigation into the elimination of port overlap with dynamometer testing of the Mazda 13B-MSP, and further considered the benefits of zero port overlap applied to a *peripherally ported* Wankel rotary engine, namely the Advanced Innovative Engineering (AIE) 225CS (7), which was being developed as a range extender within the APC project ADAPT (8, 9). Intermediate conclusions were that, whether side- or peripherally ported, the Wankel engine should be considered for range extender applications because in this role it can exploit its aforementioned headline attributes (power density, lightness, compactness, vibration-free) while inefficient operating regions can be inherently avoided. Additionally, eliminating port overlap should expand the region of best fuel consumption while offering entirely satisfactory exhaust emissions.

Item 3 is, on the face of it, difficult to avoid since Wankel engines have an inherent lack of lubrication to the combustion chamber apex seals and require direct lubrication, which is consumed, leading to an additional source of HC emissions. This concern may be tempered by again considering the excellent HC measurements on the 13B-MSP engine (4), which included any contributions from lubricating oil. Furthermore, the latest generation of UAV Wankel rotary engines employ lubrication systems that can limit oil consumption to 10 cc/hour (6), comparable to automotive engines.

[1] A brief historical overview may be found in ref. (4).

Item 4 relates to the inherent geometry of the combustion chamber in a Wankel rotary engine, where its higher surface area-to-volume ratio means that thermal losses will be greater, relative to a conventional engine. This characteristic also drives the high coolant losses mentioned in item 5, while high exhaust heat rejection is a function of the typical exhaust porting arrangement, which leads to under expansion of the working fluid when compared to a conventional engine.

Items 4 and 5 manifest themselves as lower thermal efficiency. To mitigate their impact, and to recover the performance lost due to the reduced compression and expansion ratios imposed by adopting zero port overlap, compounding the Wankel engine to extract some of the available exhaust enthalpy has also been studied. As previously reported at this conference (9), a rotary expander was designed and fitted to the exhaust of the AIE 225CS, further demonstrating the versatility of such devices. Test results demonstrated significant improvements in torque and brake specific fuel consumption (BSFC) of 30% and 12% respectively. Turbocompounding the AIE 225CS with a turbocharger turbine has also been simulated (6). This used the dedicated Wankel engine template available in AVL BOOST, which has been shown (10) to have important modelling advantages over the 'equivalent three-cylinder, four-stroke' approach that has been used elsewhere (e.g., 11).

Finally, item 6 refers to the difficulties imposed by the elongated shape of a Wankel engine combustion chamber, which does not lend itself to rapid and complete combustion of the fuel. Indeed, achieving a better understanding of the combustion process inside a Wankel rotary engine is the main objective of the current paper.

1.2 CFD modelling in Wankel rotary engines

Large-Eddy Simulation (LES) has been applied extensively for modelling turbulent flows in combustion engines, though has largely focussed on conventional reciprocating piston engines (e.g., 12). More recent work though has studied the deployment of different turbulence modelling approaches specifically for the in-chamber flow in Wankel rotary engines. A comparison of LES and a common Reynolds-averaged Navier-Stokes (RANS) technique using the standard k-ε turbulence model recommended the former for better prediction of flow field structures (13). But while LES provides a more faithful representation of turbulent flow features, it imposes significantly greater computational expense than RANS modelling. A useful compromise is provided by hybrid LES-RANS techniques, such as the Detached-Eddy Simulation (DES) approach first introduced in ref. (14). Advancements since have led to the latest hybrid models such as the Improved Delayed Detached Eddy Simulation–Shear-Stress Transport (IDDES-SST) model, which aims to balance fidelity of turbulence modelling with reasonable computational expense, with its application to a small, peripherally ported rotary engine (15). Also notable in that work is the use of the Q-criterion for turbulent feature identification.

As will be described later, this paper employs a LES approach to turbulence modelling and uses the Q-criterion (defined in Section 3.2.3) to support tracking of turbulent flow structures. The novel contribution of the present work, however, is that the four 'strokes' (intake, compression, expansion, exhaust) of a complete cycle are simulated herein, which is a notable extension beyond recent LES simulations in rotary engines (e.g., 13, 15), which were limited to the intake phase of the cycle.

2 METHODOLOGY

This section provides a brief overview of Wankel rotary engine geometry and its set-up in the CFD simulation.

2.1 Wankel rotary engine geometry

Inside a Wankel rotary engine (Figure 1a), a triangular rotor, which has a shape similar to a Reuleaux triangle (16), rotates around an output shaft and inside a trochoidal housing. The particular design shown in Figure 1 is known as a 2:3 arrangement – two housing lobes and three rotor flanks. This creates three moving chambers separated from each other by the apices of the rotor, and the internal gearing is correspondingly configured such that the output shaft rotates three times for each rotor rotation. Each chamber experiences a complete four-stroke cycle during each full rotation of the rotor, i.e., there is a combustion event upon every rotation of the output shaft.

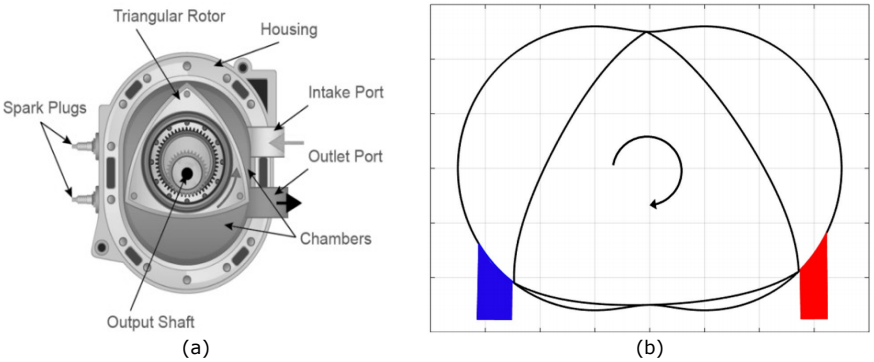

Figure 1 (a) Components of a peripherally ported rotary engine (17); (b) 2D chamber geometry with respect to intake (blue) and exhaust (red) ports for the case of zero port overlap (4)

The combustion chambers in a Wankel rotary engine are therefore continually moving and changing shape, with their boundaries defined by the eccentric motion of the rotor about the output shaft and the internal surface of the housing (Figure 1b).

2.2 CFD meshing

This subsection describes the moving and stationary mesh domains in 3D CFD. Ansys Fluent R19.2 was used for all CFD aspects described in this paper.

2.2.1 Mesh motion generation and dynamic meshing

In Fluent a moving mesh is described by a user defined function (UDF). The rotor boundary (red surface in Figure 2) is defined as a rigid wall, i.e., non-deformable. Its simultaneous translation and rotation are defined in the UDF by the velocity and angular velocity of its centre with respect to Cartesian (x,y,z) coordinates and time.

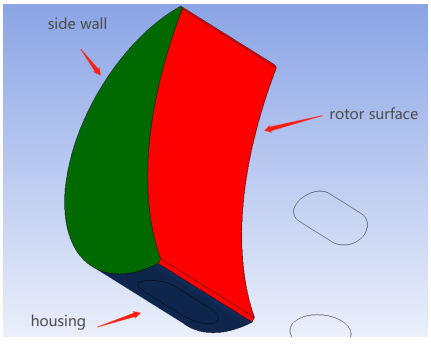

Figure 2 Rotor domain and surface boundaries

On the other hand, the required variation in chamber geometry is enacted by setting up the housing and side wall boundaries (blue and green surfaces in Figure 2) as deformable walls, whose shape adapts according to the position of the rotor.

Due to the complexity of the resulting chamber geometry, a sixth-order polynomial fit is used to describe its variation within the UDF. This is an acceptable simplification, with the difference (in the *y*-coordinate) between the actual and approximated geometries quantified by a root mean squared error of 1.14×10^{-5}. Some examples of the approximated chamber geometry are shown in Figure 3.

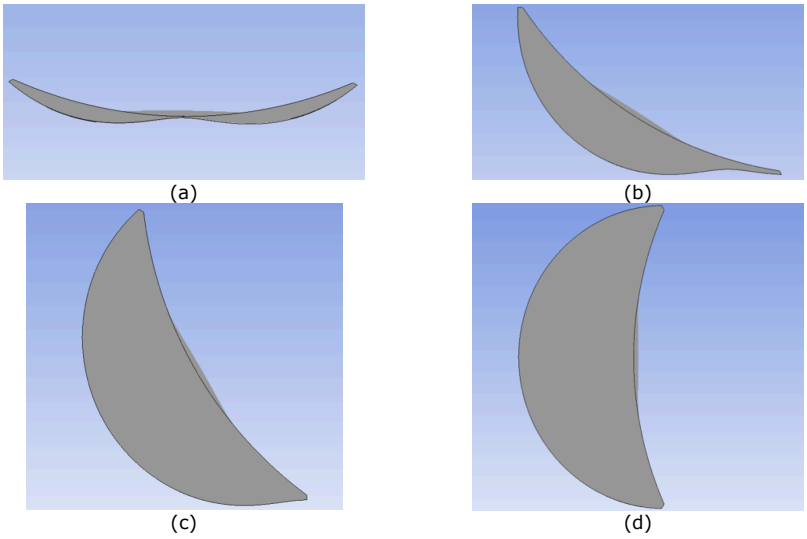

Figure 3 Combustion chamber deformation during ¼ of a rotor rotation

Meshing of the combustion chamber is challenging due to the extreme levels of cell deformation at various points in the cycle. Indeed, re-meshing is unavoidable if an acceptable cell aspect ratio is to be maintained. In this work a hybrid approach to dynamic meshing is taken, combining mesh smoothing, and manual and automatic re-meshing, the latter employing Fluent's cut-cell functionality.

The cut-cell feature automatically re-meshes the domain with an unstructured hexahedral mesh, which offers a significantly lower cell count compared to a tetrahedral mesh, while permitting a level of flexibility unavailable in a fully structured mesh. The main drawback, however, is that automatic re-meshing does not recreate the intended geometry with complete accuracy. In addition, the more often automatic re-meshing is used, the less faithful the mesh becomes. Figure 4 shows this situation following multiple calls for automatic re-meshing. In Figure 4b, the curvature of the rotor surface has changed. Although only slight, this will eventually have a material effect on chamber volume at top dead centre (TDC) and therefore the simulated geometrical compression ratio, and hence the accuracy of the predicted performance. For these reasons, a sensible balance between user time and geometrical accuracy was found by invoking automatic re-meshing once every 1/30 of a cycle, with manual mesh replacement (which corrects any geometrical inaccuracy) performed once every 1/12 of cycle.

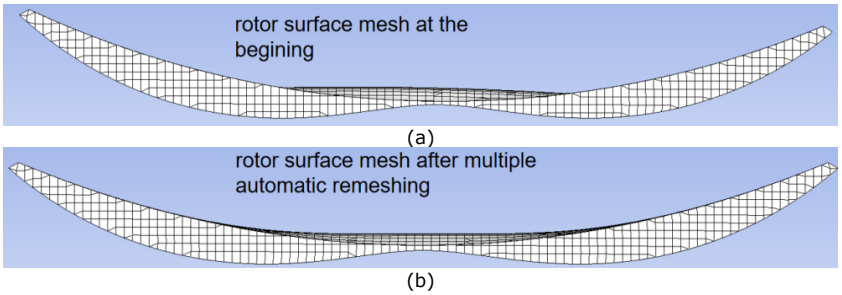

Figure 4 Combustion chamber mesh at (a) beginning of simulation; (b) after multiple instances of automatic re-meshing

In between re-meshing events, the mesh deforms with Fluent's smoothing option. This seeks to retain mesh quality by diffusing the movement smoothly into every node, as Figure 5 shows (N.B. the boundary mesh is purposely refined due to high velocity and temperature gradients in these regions).

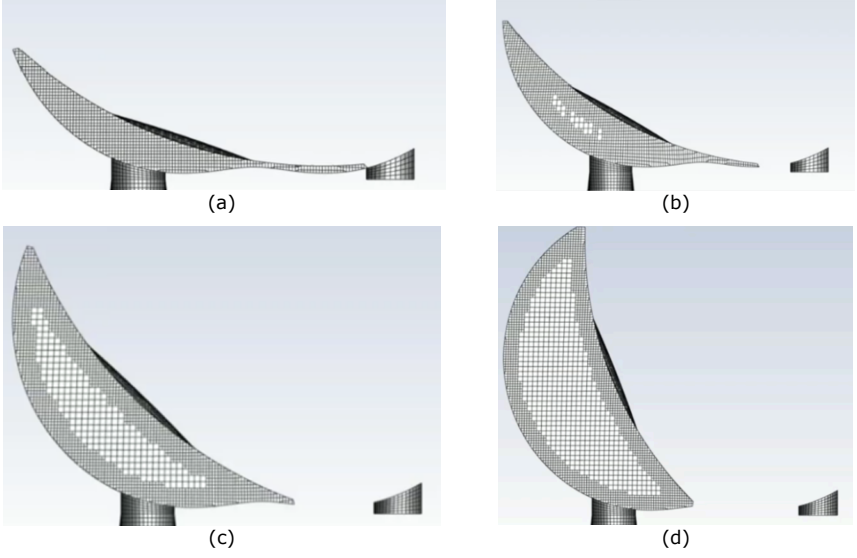

Figure 5 Smooth mesh deformation

It is worth noting that the cell count in the chamber domain varies between approximately 60,000–100,000, depending on the complexity of the deforming domain and dictated by the dynamic meshing technique just described. For the sake of brevity, the mesh dependency study is not reported in this paper. Suffice to say, this order of mesh resolution is in line with the observation in ref. (13) that there is little to choose in the quality of CFD validation between cell counts of 100,000 and 1,000,000 elements, especially considering the computational expense of the latter.

2.2.2 Intake and exhaust domains

A hexahedral mesh is applied to the remaining stationary domains of the intake and exhaust systems. The intake domain (Figure 6a) includes a representation of the throttle, meshed using tetrahedral elements since it is important to capture its effect on the flow structures and turbulence level entering the combustion chamber. The exhaust domain (Figure 6b) is directly modelled on the one attached to the 225CS during the aforementioned engine testing, with a grid that becomes purposely more coarse as the distance from the combustion chamber and exhaust port increases.

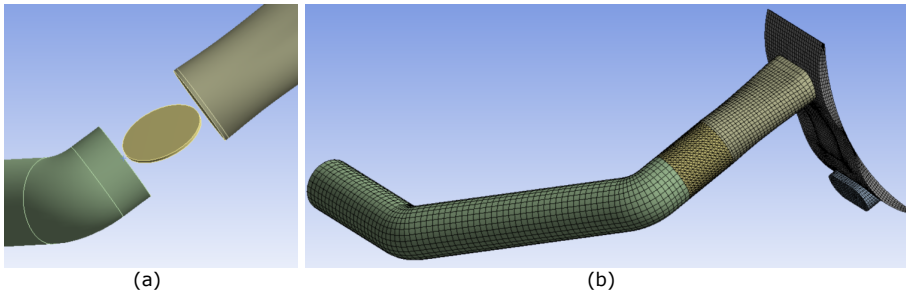

(a) (b)

Figure 6 (a) Intake throttle representation; (b) exhaust system mesh

2.2.3 Leakage

It is well known (e.g., 18, 19) that gas leakage across the apex seals detrimentally affects Wankel engine performance. A side study (not included here for brevity) attempted to simulate this leakage path, using a minimum apex gap of 0.5 mm due to the computational expense of the required fine mesh. This predicted unrealistically large leakage levels. Hence the CFD model, at present, assumes no leakage.

2.2 CFD set-up

This section describes simulation set-up in Ansys Fluent R19.2.

2.2.2 LES model

Preparatory simulation work (not reported here) was carried out by the authors to compare RANS and LES modelling approaches to the problem. As suggested in other work (13), this identified the value of the latter in being able to capture with sufficient fidelity the flow structures entering the combustion chamber and their subsequent breakdown into turbulence, thus obtaining a more valid model of the combustion process occurring within a Wankel engine. Unlike the RANS approach, which purposely averages out all turbulence structures and cannot resolve at the eddy scale, LES is capable of resolving eddies larger than eight cells (i.e., a cube with side length equal to two cells). For turbulence structures smaller than eight cells, the simulation will switch to a sub-grid model that is similar to a RANS approach.

2.2.2 Simplified combustion model

The combustion modelling approach employed in this work used Ansys Fluent's built-in *Spark Model*. This creates a local reaction hotspot for user-defined values of position, point in time, and initial conditions for hotspot radius (in this case 2 mm) and energy release (in this case 0.05 J); these parameters were tuned to best match the experimental result. The combustion process itself is very much simplified, using a finite-rate reaction model and a single reaction for iso-octane fuel (Eq. (1)):

$$C_8H_{18} + 12.5\,O_2 \longrightarrow 8\,CO_2 + 9\,H_2O \qquad (1)$$

2.2.3 Wall heat transfer

As explained in Section 1.1, compared to reciprocating engines, the Wankel engine suffers from higher heat losses through the wall due to its high surface area-to-volume ratio, particularly around TDC (e.g., 18, 19). Wall heat transfer is thus a key factor affecting both work output and thermal efficiency. In the current study, all walls are set to 90°C, in line with the coolant temperature measured during engine testing (and since no direct wall temperature measurements were made). However, a side study (not included here for conciseness but which applied temperatures of 60°C and 120°C) showed that the assumed wall temperature had little impact on simulation results. Although prescribing a single temperature value to all walls is an overly simplified approach, there are additional reasons that prohibit the simulated wall heat transfer being wholly representative of the real situation:

- Due to the way in which the combustion chamber moving mesh is generated, the internal wall of the housing effectively moves with the chamber, whereas it is stationary in reality. This reduces the relative velocity between the gas and the wall and hence the rate of convective heat transfer.
- To accurately simulate wall heat transfer, the near-wall mesh would need to be much finer than could be afforded here.

2.3 Engine testing

As previously mentioned, the subject engine of this paper is the production single-rotor 225CS Wankel rotary engine (7), designed and manufactured by Advanced Innovative Engineering. Its main geometric and timing details are listed in Table 1. The 225CS is port fuel injected, with the injector purposely angled to direct the fuel through the port and into the combustion chamber (Figure 7).

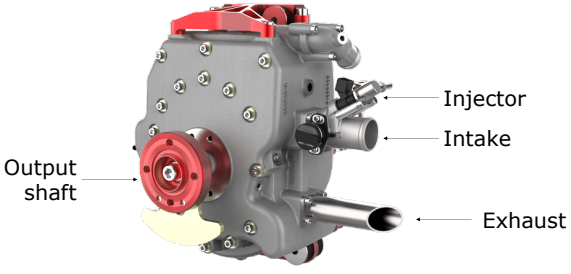

Figure 7 The AIE 225CS Wankel rotary engine (7)

Table 1 AIE 225CS engine geometry and timing (9)

Parameter	Value	Units
Swept volume	225	cc
Generating radii	69.5	mm
Eccentricity	11.6	mm
Offset/equidistance	2	mm
Rotor number	1	
Width of rotor housing	51.941	mm
Geometric compression ratio	9.6:1	
Intake port opens	71 BTDC	°
Intake port closes	60 ABDC	°
Exhaust port opens	69 BBDC	°
Exhaust port closes	57 ATDC	°
Number of spark plugs	2	
Ignition timing	18 BTDC	°

Data to be used for CFD validation was compiled from steady-state engine dynamometer testing conducted at the University of Bath as part of the Advanced Propulsion Centre and Innovate UK-funded project ADAPT (8). In a reciprocating piston engine, a single pressure sensor can be installed in the head to measure combustion chamber pressure. In a Wankel engine however, owing to its rotating chambers, multiple pressure sensors are required to capture a complete pressure trace over a full rotor rotation, and the corresponding data concatenated in post-processing. A live data acquisition system was designed and developed (20) for use with Wankel engines that could generate in-chamber pressure traces and *p-V* diagrams without post-processing. The details of this technique are outside the scope of the current paper, but a full explanation and analysis can be found in refs. (4, 6).

3 RESULTS & DISCUSSION

3.1 CFD validation

This section demonstrates validation of the 3D CFD model against both motored and fired engine test data, for high-load engine operation at 4000 rpm.

3.1.1 Comparison of chamber pressure: motored operation

A comparison of predicted and measured combustion chamber pressure for motored operation (i.e., without combustion) is shown in Figure 8, with the throttle position at approximately 93% open. It can be observed that there is very good correlation between the simulation and experimentally measured data.

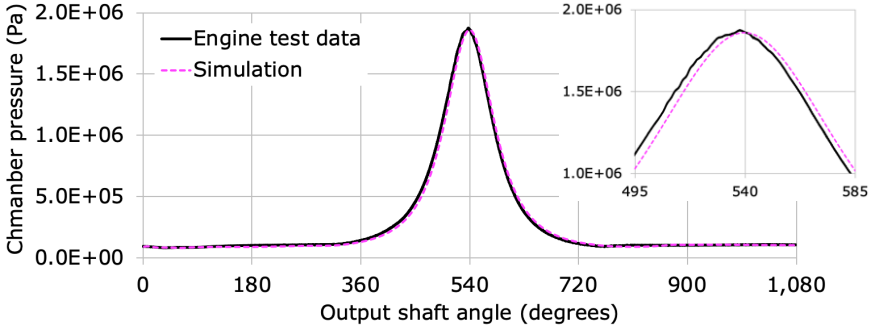

Figure 8 Comparison of experimentally measured and simulated chamber pressure during motored operation at 4000 rpm and 93% throttle opening

In the engine test, *brake* torque is measured by the dynamometer, whereas the CFD simulation can only calculate an *indicated* torque quantity (i.e., that due to the pressure forces on the rotor over a cycle). By calculating the difference between these two values, and although they are taken from different sources (experiment and simulation), one may estimate the magnitude of mechanical friction torque present in the 225CS engine at this operating point. Table 2 shows this breakdown of torque values, resulting in an estimated mechanical friction torque of -3.69 Nm.

Table 2 Estimate of mechanical friction torque using measured and simulated data for the motored case

Type of torque	Data source	Value	Units
Dynamometer torque (i.e., accounts for mechanical friction and pumping losses)	Engine test	-4.0	Nm
Indicated pumping torque	Simulation	-0.31	Nm
Estimated mechanical friction torque	Combines engine test and simulation	-3.69	Nm

3.1.2 Comparison of chamber pressure: fired operation

Next, Figure 9 compares engine test data and CFD predictions of the chamber pressure for a fired (i.e., with combustion) case, again at 4000 rpm and 93% throttle opening. There remains a good correlation overall, but a few regions of difference.

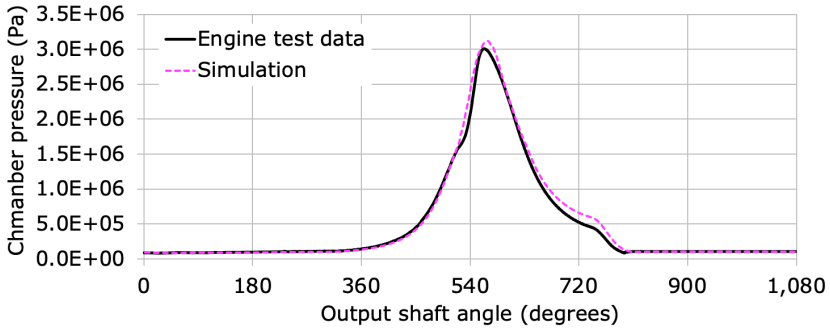

Figure 9 Comparison of experimentally measured and simulated chamber pressure during fired operation at 4000 rpm and 93% throttle opening

The pressure rise in the simulation trace is smooth, but the engine test data shows a decrease in gradient at around 520° output shaft angle, which would coincide with the ignition timing (set at 18° BTDC, as per Table 1). It is surmised that this difference is caused by a mixture of fuel vaporization (not modelled in the simulation) and a transition to a much faster pressure rise rate due to the start of combustion.

The engine test and simulation pressure traces peak at 558° and 568° output shaft angle (18° and 28° ATDC) respectively, with the simulation showing a slightly greater peak pressure (by ~3.7%). This is likely due to the presence of greater thermal losses in the engine test data than are being accounted for in the simulation. The engine test data also shows a faster decrease in pressure from approximately 640°, leading to a pressure difference of approximately 36% by the point at which the exhaust port is uncovered, at about 750° output shaft angle.

3.2 Combustion chamber flow phenomena

Having shown that the 3D CFD simulations provide a faithful model of the 225CS engine in performance terms, the CFD-predicted flow structures are now examined by considering, e.g., the velocity field and turbulent viscosity levels.

3.2.1 Flow structures during intake stroke

The flow structures during the intake 'stroke' are important for generating the turbulence that will later promote rapid and clean combustion.

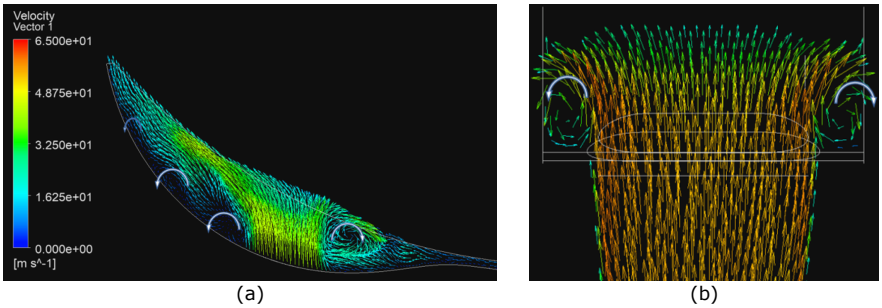

(a) (b)

Figure 10 (a) Chamber, (b) intake velocity vectors; 72° output shaft angle

Figure 10 shows velocity vectors for the point at which the output shaft is at 72° and the chamber is quite elongated. It shows formation of vortices as the gas enters the chamber (Figure 10a) from the intake (Figure 10b), before striking the rotor surface.

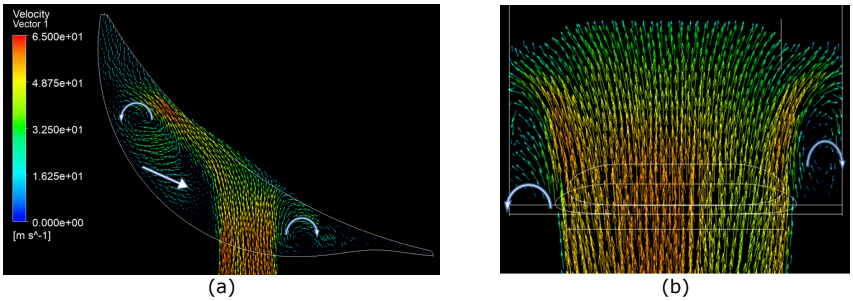

(a) (b)

Figure 11 (a) Chamber, (b) intake velocity vectors; 108° output shaft angle

As the chamber starts to expand in Figure 11 (108° output shaft angle), small eddies merge into larger ones near the rotor leading edge. But as the chamber expands further, and the intake flow starts to slow down (Figure 12), the large vortex near the leading edge starts to break into multiple smaller vortices. Meanwhile, the vortex near the trailing edge is sustained noticeably longer due to its relative isolation.

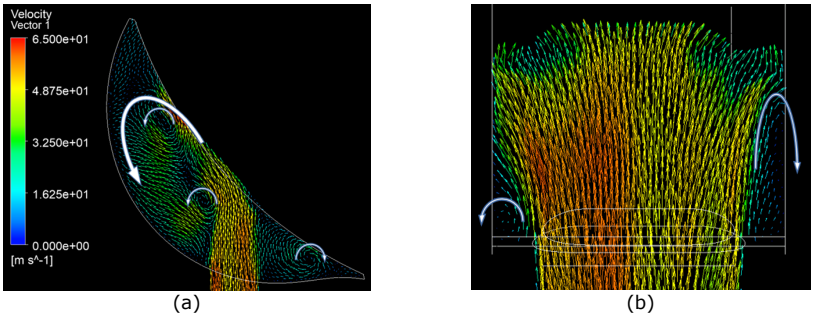

(a) (b)

Figure 12 (a) Chamber, (b) intake velocity vectors; 144° output shaft angle

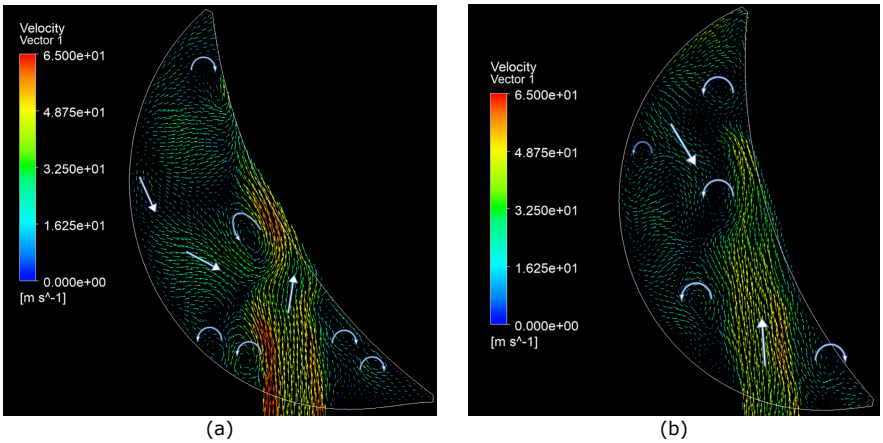

(a) (b)

Figure 13 Chamber velocity vectors, (a) 180° & (b) 216° output shaft angle

As the intake stroke ends (Figure 13), the flow quickly starts to decelerate, and the vortices start to break down.

3.2.2 Flow structures during compression stroke

As the chamber begins to shrink again during the compression stroke (Figure 14), the vortices quickly break down because there is insufficient space to sustain large scale rotation. Just before ignition occurs (Figure 14c), almost all vortices have broken down to such a small size that they cannot be resolved directly due to the finite resolution of the mesh, at which point the sub-grid model takes over.

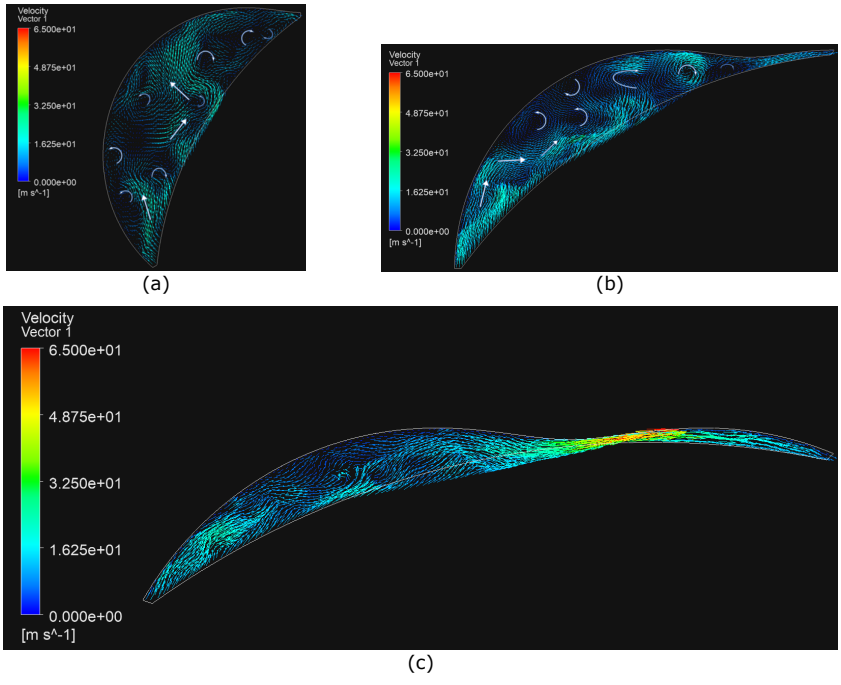

Figure 14 Chamber velocity vectors at output shaft angles of (a) 360°, (b) 450°, & (c) 522°

3.2.3 Turbulence tracking

To visualize the turbulence levels, the so-called Q-criterion is introduced (Eq. (2),

$$Q = \frac{1}{2}(\|\boldsymbol{\Omega}\|^2 - \|\mathbf{S}\|^2) \tag{2}$$

where $\mathbf{S}$ is the symmetric part of the velocity gradient (better known as the rate of strain), and $\boldsymbol{\Omega}$ is its antisymmetric part, otherwise known as the vorticity tensor. The Q-criterion is automatically available within the Ansys post-processing tool (CFD-Post). Further details of the Q-criterion can be found in the literature (e.g., 15, 21), but essentially, a higher Q-criterion indicates a region is dominated more by vorticity than strain. For example, the Q-criterion will increase towards the centre of a vortex – indeed, a local Q-criterion hotspot can aid vortex detection, as Figure 15 shows.

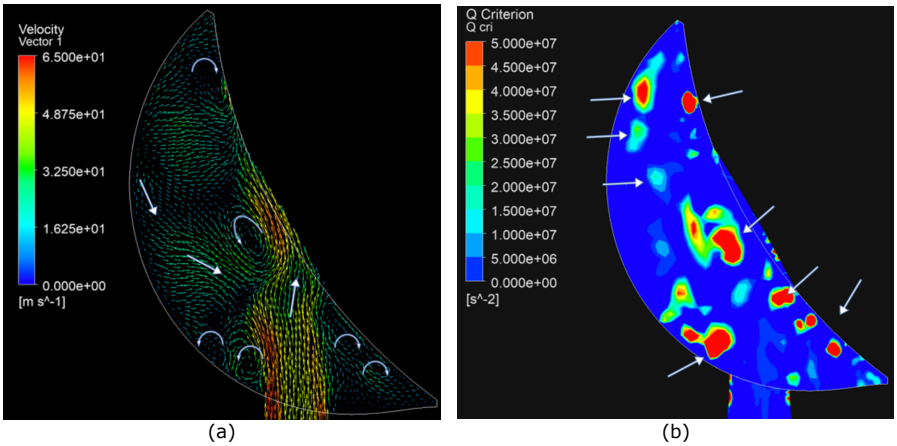

(a) (b)

Figure 15 Identifying vortical structures (a) as Q-criterion hotspots (b)

The LES sub-grid model is also introduced for comparison. As previously explained, LES is able to resolve large scale eddies, but when they reduce to a scale smaller than a cube with a side length of two cells, the sub-grid model will be activated. More specifically, this means the local viscosity and thermal conductivity are increased to represent the turbulence level, similar to a RANS approach. And since the very centre of a vortex must be smaller than any finite mesh size, the sub-grid viscosity will increase at the vortex core, much like the Q-criterion.

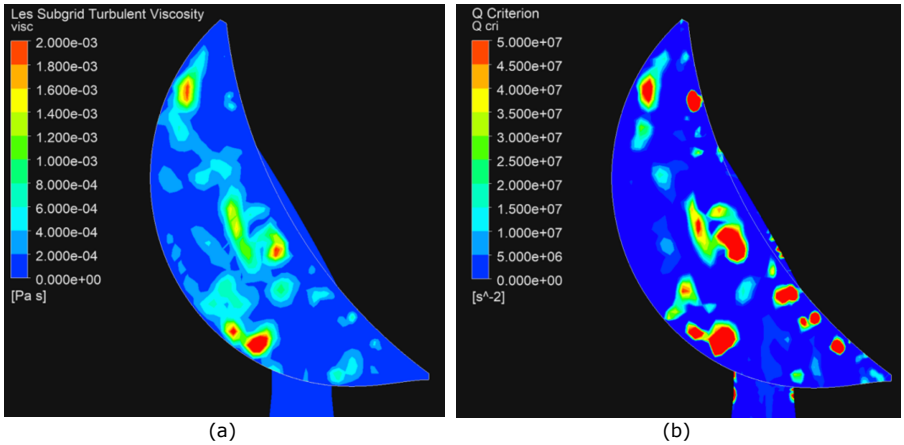

(a) (b)

Figure 16 Comparing contours of sub-grid viscosity (a) & Q-criterion (b)

As Figure 16 shows, there is clear similarity between the contours of the LES sub-grid turbulence viscosity and Q-criterion. However, LES sub-grid turbulence viscosity is highly affected by mesh density, and since the sub-grid model only activates when the mesh size is too large relative to the turbulence, it is only comparable to itself when the mesh density is uniform – which is definitely not the case in this work. Indeed, it can be seen in Figure 16a that near the rotor surface, where the mesh is finer, the LES sub-grid turbulent viscosity is at a low level, whereas Figure 16b suggests small hotspots of vorticity are, in fact, present. In conclusion, the Q-criterion is the better identifier of vortices for the purposes of the present work.

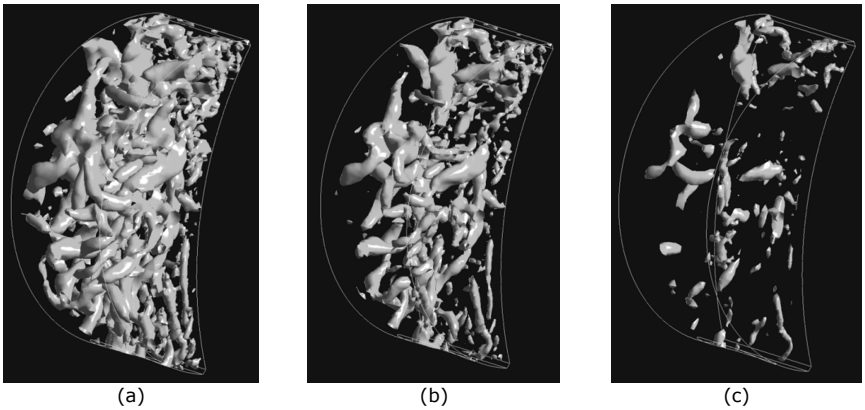

(a) (b) (c)

Figure 17 Q-criterion iso-surfaces: (a) 1 x 10^7, (b) 2 x 10^7, & (c) 5 x 10^7 s^{-2}

Taking this a step further, Q-criterion iso-surfaces can help define the shape of vortices in 3D space, as Figure 17 shows. The higher the iso-surface setting, the tighter it envelopes a vortex core, and so eventually only the most intense vortices will remain. In this case, a Q-criterion iso-surface set to 2 x 10^7 s^{-2} (as per Figure 17b) offers a balance between showing the quantity of coherent structures present while permitting individual vortices to be identified.

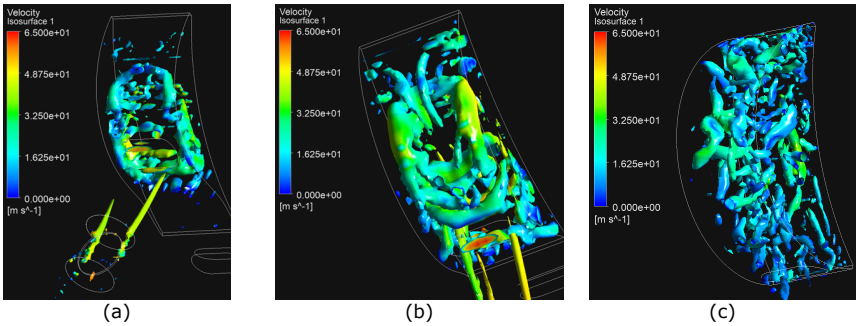

(a) (b) (c)

Figure 18 Velocity-coloured Q-criterion = 2 x 10^7 s^{-2} iso-surfaces during the intake stroke

The (velocity-coloured) 3D Q-criterion iso-surfaces in Figure 18 identify two strong vortices generated by the throttle plate (visible in Figure 18a), which are sustained through the intake port but dissipate upon entering the chamber (Figure 18b). As the intake stroke continues, the maximum vortex length scale is attained at an output shaft angle of approximately 160°. As the intake stroke proceeds, the flow starts to slow down, and the large vortices start to break up into multiple vortices of smaller scale (Figure 18c).

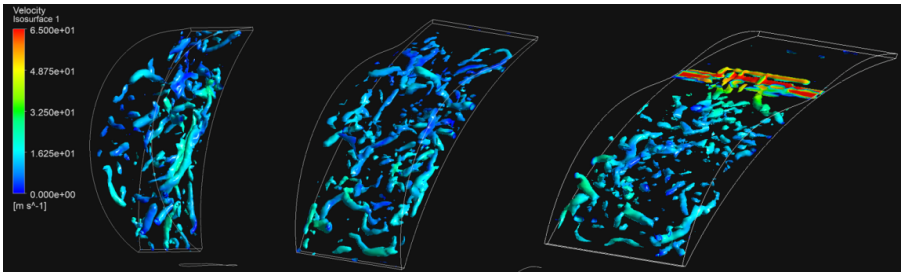

Figure 19 Velocity-coloured Q-criterion = 2 x 10^7 s^{-2} iso-surfaces between compression and ignition

As the intake port closes (left hand side of Figure 19), the vortices start to dissipate and reduce in length scale. Nevertheless, a large number of small vortices persist just in advance of ignition (right hand side of Figure 19) – which will support the development of the flame once the charge ignites.

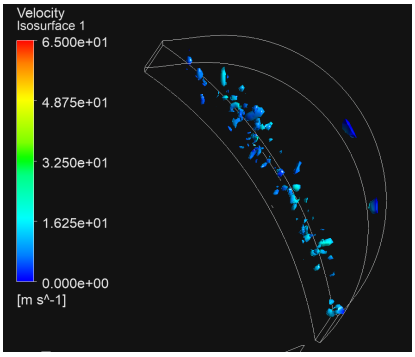

Figure 20 Velocity-coloured Q-criterion = 2 x 10^7 s^{-2} iso-surfaces during expansion

Following ignition, and moving into the expansion stroke, most vortices have dissipated, with very few, smaller vortices observed near the rotor surface (Figure 20), which could also be attributed to movement of the rotor.

3.2.4 Flame structure

The very simplified single-equation representation of combustion (Eq. (1)) prohibits tracking of intermediate species, which include those used as accepted markers of the flame front, e.g., OH, C_2, CH, CH_2O (22, 23). The combustion model will be upgraded in future, but here visualization of the flame structure in 3D space is achieved by monitoring the mass fraction of CO_2 as an end product of combustion.

The flame is ignited once the two spark plugs strike at 18° BTDC (522° output shaft angle) and the two corresponding flame fronts spread out quickly (Figure 21a) and merge near TDC (Figure 21b). The flame reaches the leading edge of the rotor at approximately 36° ATDC (576° output shaft angle) in Figure 21c. However, even with the space afforded by the flank cut-out, the flame front has difficulty in passing into the narrow gap formed between the flank and housing. These results in an unburnt pocket near the trailing edge of the rotor, visible in in Figure 21d. This remains unburnt even after the exhaust stroke begins (Figure 21f) because the flame spreads at a rate slower than the chamber expands and is likely to be a major contributor to the engine's total HC emissions.

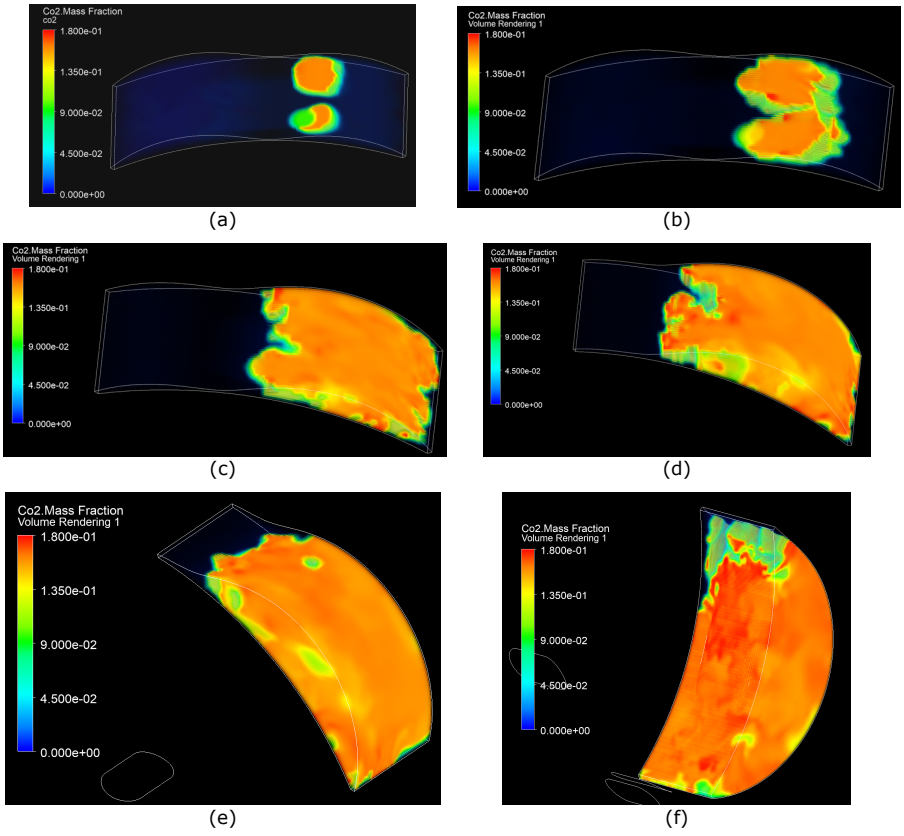

Figure 21 CO_2 mass fraction contours at output shaft angles of (a) 530°, (b) 540°, (c) 576°, (d) 612°, (e) 648°, & (f) 900°

4 CONCLUSIONS

Despite the growing electrification of transport, internal combustion engines will persist for many decades to come. It is thus crucial to continue improving the thermal efficiency of engines, and reduce CO_2 and pollutant emissions, not least because they are an important part of the transition, in the form of range-extended electric vehicles. The Wankel rotary engine offers most of the characteristics of the ideal hybrid propulsion system prime mover (e.g., compactness, lightness, excellent NVH) but the continually changing chamber shape leads to combustion inefficiencies. To better understand their cause, the overall aim of this work was to develop a realistic model of the in-chamber turbulent flow and combustion processes.

A Large-Eddy Simulation (LES) model of the deforming combustion chamber inside a Wankel rotary engine has been successfully validated against engine performance test results. The complete intake-compression-expansion-exhaust cycle is simulated, an important extension beyond other LES simulations of rotary engines in the literature, which mainly focus on the intake phase. In this work, where mesh resolution is at a premium, a hybrid (manual/automatic) approach to dynamic meshing has been deployed in the 3D CFD simulations in order to keep the mesh count to reasonable levels, while maintaining resolvability of turbulent flow features. Furthermore, the Q-criterion has been shown to be a more reliable indicator of local

turbulence levels than the LES sub-grid turbulent viscosity. The LES modelling approach, in conjunction with the Q-criterion, can be used to better understand the combustion process in the continually deforming combustion chamber. It allows the turbulent flow structures to be tracked throughout the intake and compression strokes, demonstrating that they persist, albeit at a reducing length scale, until at least the start of combustion. Tracking the extent of the flame following ignition, and into the expansion and exhaust strokes, identified regions at the rotor trailing edge into which the flame cannot reach – leading to a pocket of unburnt reactants. Hence this paper underscores the importance of Wankel engine intake geometry in generating turbulence that, crucially, is available at the beginning of the combustion process to promote rapid flame development. It also emphasizes the inherent difficulties posed by Wankel engine combustion chamber geometry on flame propagation. Indeed, the influence of spark plug location and ignition timing on the size and persistence of unburnt regions will be the subject of future work in this area.

ACKNOWLEDGMENTS

The authors would like to thank the Advanced Propulsion Centre and Innovate UK for their financial support of APC6 Project 113127: ADAPT-IPT "Reducing Vehicle Carbon Emissions through Development of a Compact, Efficient, and Intelligent Powertrain" (8). The authors would also like to very much thank Kristina Burke for her project management of the ADAPT-IPT programme.

REFERENCE LIST

1. Advanced Propulsion Centre (2020) "Light Duty Vehicle <3.5t – Propulsion Technologies Roadmap", Automotive Council UK and Advanced Propulsion Centre UK 2020 Product Roadmaps, URL: https://www.apcuk.co.uk/product-roadmaps, last accessed 2021-08-21.
2. Mock, P. & Diaz, S. (Eds) (2020) "European Vehicle Market Statistics — Pocketbook 2020/21", International Council on Clean Transportation Europe, URL: http://eupocketbook.theicct.org, last accessed 2021-08-21.
3. Weymar, E. & Finkbeiner, M. (2016) "Statistical analysis of empirical lifetime mileage data for automotive LCA", *Int. J. Life. Cycle. Assess.*, **21**(2016), 215-223. doi:10.1007/s11367-015-1020-6
4. Turner, J.W.G., Turner, M., Vorraro, G. & Thomas, T. (2020) "Initial Investigations into the Benefits and Challenges of Eliminating Port Overlap in Wankel Rotary Engines", SAE Technical Paper 2020-01-0280. doi:10.4271/2020-01-0280
5. Ohkubo, M., Tashima, S., Shimizu, R., Fuse, S. & Ebino, H. (2004) "Developed Technologies of the New Rotary Engine (RENESIS)", SAE Technical Paper 2004-01-1790. doi:10.4271/2004-01-1790
6. Turner, J.W.G., Turner, M., Islam, R., Shen, X. & Costall, A. (2020) "Further Investigations into the Benefits and Challenges of Eliminating Port Overlap in Wankel Rotary Engines", SAE Technical Paper 2021-01-0638. doi:10.4271/2020-01-0280
7. Advanced Innovative Engineering (2021) "Wankel Rotary Engine 225CS 40BHP", Product Datasheet, URL: https://www.aieuk.com/225cs-40bhp-wankel-rotary-engine, last accessed 2021-08-21.
8. Advanced Propulsion Centre (2018) "Westfield – ADAPT: Reducing Vehicle Carbon Emissions through Development of a Compact, Efficient, and Intelligent Powertrain", URL: https://www.apcuk.co.uk/portfolio/westfield-adapt, last accessed 2021-08-21.
9. Vorraro, G., Islam, R., Turner, M. & Turner, J.W.G. (2019) "Application of a Rotary Expander as an Energy Recovery System for a Modern Wankel Engine",

In Proc. Inst. Mech. Eng. Int. Conf. on Internal Combustion Engines and Powertrain Systems for Future Transport (ICEPSFT 2019), Birmingham, UK, 11–12 December, 260-282.
10. Peden, M., Turner, M., Turner, J.W.G. & Bailey, N. (2018) "Comparison of 1-D Modelling Approaches for Wankel Engine Performance Simulation and Initial Study of the Direct Injection Limitations", SAE Technical Paper 2018-01-1452. doi:10.4271/2018-01-1452
11. Tartakovsky, L., Baibikov, V., Gutman, M., Veinblat, M. & Reif, J. (2012) "Simulation of Wankel Engine Performance Using Commercial Software for Piston Engines", SAE Technical Paper 2012-32-0098. doi:10.4271/2012-32-0098
12. Celik, I., Yavuz, I. & Smirnov, A. (2001) "Large eddy simulations of in-cylinder turbulence for internal combustion engines: A review", *Int. J. Engine Res.* **2**(2), 119-148. doi:10.1243/1468087011545389
13. Poojitganont, T., Sinchai, J., Watjatrakul, B. & Berg, H. P., (2019) "Numerical Investigation of In-chamber Flow inside a Wankel Rotary Engine", *IOP Conf. Ser.: Mater. Sci. Eng.* **501** (2019), 012043. doi:10.1088/1757-899X/501/1/012043
14. Spalart, P. R., Jou, W.-H., Strelets, M. & Allmaras, S. R. (1997) "Comments on the Feasibility of LES for Wings, and on a Hybrid LES/RANS Approach", *In* Proc. First AFOSR Int. Conf. on DNS/LES, 137-147.
15. Zhang, Y., Liu, J. & Zuo, Z. (2018) "The Study of Turbulent Fluctuation Characteristics in a Small Rotary Engine with a Peripheral Port Based on the Improved Delayed Detached Eddy Simulation Shear-Stress Transport (IDDES-SST) Method", *Energies* **11**(3), 642. doi:10.3390/en11030642
16. Martini, H., Montejano-Peimbert, L. & Braniff Oliveros, D. (2019) 'Bodies of Constant Width: An Introduction to Convex Geometry with Applications', Birkhäuser (Basel). doi:10.1007/978-3-030-03868-7
17. Wankel Supertec GmbH (2015) "General Information about Rotary Engines", Web page, URL: https://www.wankelsupertec.de/en_rotary_engines.html, last accessed 2021-08-21.
18. Feller, F. (1970) 'The 2-Stage Rotary Engine–A New Concept in Diesel Power', Proc. Inst. Mech. Eng. **185**(1), 139-158. doi:10.1243/PIME_PROC_1970_185_022_02
19. Yamamoto, K. (1981) 'Rotary Engine', Sankaido (Tokyo).
20. Vorraro, G., Turner, M. & Turner, J.W.G. (2019) "Testing of a Modern Wankel Rotary Engine – Part I: Experimental Plan, Development of the Software Tools and Measurement Systems", SAE Technical Paper 2019-01-0075. doi:10.4271/2019-01-0075
21. Zhan, J.-M., Li, Y.-T., Onyx Wai, W.-H. & Hu, W.-Q. (2019) "Comparison between the Q Criterion and Rortex in the Application of an In-stream Structure", *Phys. Fluids* **31**, 121701. doi:10.1063/1.5124245
22. Pfadler, S., Beyrau, F. & Leipertz, A. (2007) "Flame front detection and characterization using conditioned particle image velocimetry (CPIV)", *Opt. Express* **15**(23), 15445-15456. doi:10.1364/OE.15.015444
23. Liu, X., Kokjohn, S., Wang, H. & Yao, M. (2019) "A comparative numerical investigation of reactivity controlled compression ignition combustion using Large Eddy Simulation and Reynolds-Averaged Navier-Stokes approaches", *Fuel* **257**, 116023. doi:10.1016/j.fuel.2019.116023